Precipitation of Relativistic Electrons Under Resonant Interaction with Electromagnetic Ion-Cyclotron Wave Packets

Veronika, S. Grach[1,1] and Andrei, G. Demekhov[1,1]

[1]Institute of Applied Physics, Russian Academy of Sciences

November 30, 2022

Abstract

We use numerical simulations to study the resonant interaction of relativistic electrons with rising-frequency EMIC wave packets in the H band. We find that precipitation fluxes are formed by quasi-linear interaction and several nonlinear interaction regimes having opposite effects. In particular, the influence of Lorentz force on the particle phase (force bunching) decreases precipitation for particles with low equatorial pitch angles (up to 15-25), and can even block it completely.

Four other nonlinear regimes are possible: nonlinear shift of the resonance point (can cause pitch angle drift in both directions); phase bunching (slightly increases pitch angle for untrapped particles); directed scattering (strongly decreases pitch angle for untrapped particles) and particle trapping by the wave field (decreases pitch angle). Equatorial pitch angle distribution evolution during several passes of particles through the wave packet is studied. The precipitation fluxes are evaluated and compared with theoretical estimates.

We show that strong diffusion limit is maintained for a certain range of energies by a wave packet with realistic amplitude and frequency drift. In this case, the quasi-linear theory strongly underestimates the precipitated flux. With increasing energy, the precipitated fluxes decrease and become close to the quasi-linear estimates.

Precipitation of Relativistic Electrons Under Resonant Interaction with Electromagnetic Ion-Cyclotron Wave Packets

V. S. Grach[1] **and A. G. Demekhov**[2,1]

[1]Institute of Applied Physics, Russian Academy of Sciences
[2]Polar Geophysical Institute
[1]46, Ul'yanov st., 603950, Nizhny Novgorod, Russia
[2]26a, Academgorodok st., 184209, Apatity, Russia

Key Points:

- Nonlinear resonant interaction with EMIC waves can either increase or decrease electron pitch angle
- For some energies pitch angle distribution stays isotropic, precipitating fluxes at strong diffusion limit
- For higher energies precipitating fluxes correspond to weak diffusion and agree with quasi-linear theory

Corresponding author: V.S. Grach, vsgrach@ipfran.ru

Abstract

We use numerical simulations to study the resonant interaction of relativistic electrons with rising-frequency EMIC wave packets in the H^+ band. We find that precipitating fluxes are formed by quasi-linear interaction and several nonlinear interaction regimes having opposite effects. In particular, the direct influence of Lorentz force on the particle phase (force bunching) decreases precipitation for particles with low equatorial pitch angles (up to 15–25°), and can even block it completely. Four other nonlinear regimes are possible: nonlinear shift of the resonance point which can cause pitch angle drift in both directions; phase bunching that slightly increases pitch angle for untrapped particles; directed scattering that strongly decreases pitch angle for untrapped particles, and particle trapping by the wave field that decreases pitch angle. The evolution of the equatorial pitch-angle distribution during several passes of particles through the wave packet is studied. The precipitating fluxes are evaluated and compared with theoretical estimates. We show that strong diffusion limit is maintained for a certain range of energies by a wave packet with realistic amplitude and frequency drift. In this case, the quasi-linear theory strongly underestimates the precipitating flux. With increasing energy, the precipitating fluxes decrease and become close to the quasi-linear estimates.

1 Introduction

The loss of relativistic radiation belt electrons has been observed and studied theoretically for a number of years (Thorne & Kennel, 1971; Millan & Thorne, 2007; Morley et al., 2010; Engebretson et al., 2015). The resonant interaction of relativistic electrons with electromagnetic ion-cyclotron (EMIC) waves is believed to be one of the main causes of this precipitation.

Initially, resonant interaction of relativistic electrons with EMIC waves has been analyzed within the framework of the quasi-linear theory (Summers & Thorne, 2003; Jordanova et al., 2008; Shprits et al., 2009). However, along with the noise bursts of EMIC waves, quasi-monochromatic wave packets (pearls or hydromagnetic chorus emissions) with frequencies of several Hz are often observed and their amplitudes, even moderate ones, can be high enough to ensure strongly nonlinear interaction (Kangas et al., 1998; Demekhov, 2007; Engebretson et al., 2007; Engebretson et al., 2008; Pickett et al., 2010). Pearl emissions (periodic sequences of quasi-monochromatic wave packets with periods about 100 s and increasing frequency inside each packet) are explained by a passive mode locking regime of the ion cyclotron instability (Belyayev et al., 1984; Belyaev et al., 1987; Demekhov, 2007; Trakhtengerts & Rycroft, 2008). Hydromagnetic chorus emissions or EMIC triggered emissions (Pickett et al., 2010) are similar in structure to whistler mode (ELF/VLF) chorus emissions (e.g. (Santolik et al., 2003)), and they are probably generated by a similar mechanism (Trakhtengerts, 1995). Nonlinear models of hydromagnetic chorus emissions were developed by Trakhtengerts and Demekhov (2007); Omura et al. (2010); Shoji et al. (2011). It is also worth noting that the observed loss of the outer radiation belt (Morley et al., 2010) can be too fast to be explained by quasi-linear diffusion rates.

Albert and Bortnik (2009) analyzed nonlinear interaction of relativistic electrons with an EMIC wave with a constant frequency. They showed the possible role of two nonlinear regimes: phase bunching without trapping, which leads to rapid pitch angle increase and thus can decrease the precipitating flux, and particles trapping by the wave field, which results in decreasing pitch angle. Artemyev et al. (2015) showed that trapping by the EMIC wave is stable with respect to non-resonant magnetic field fluctuations.

Nonlinear interaction of relativistic electrons with a model EMIC wave packet, corresponding to the emission with rising frequency, has been studied through theoretical analysis and test particle simulations in (Omura & Zhao, 2012, 2013; Kubota & Omura,

2017; Grach & Demekhov, 2018a, 2018b). Kubota and Omura (2017) showed that combined scattering process of the nonlinear wave trapping and another nonlinear regime 'SLPA' (Scattering at Low Pitch Angle) can lead to the rapid loss of relativistic electrons. The authors explained 'SLPA'-regime by the Lorentz force term in the equation for the particle phase (hereafter termed force bunching).

Grach and Demekhov (2018a, 2018b) have shown that a strong non-diffusive decrease of the pitch angle of untrapped electrons can also occur for fairly high pitch angles. This effect, called directed scattering, is not related to the force bunching and occurs for a small group of particles that spend a long time near the separatrix on the phase plane far from the saddle point, i.e., in the region where the phase is opposite to the phase-bunched particles.

Long time evolution of particle distribution function as a result of nonlinear resonant interaction with a monochromatic wave (various modes) was studied by Artemyev et al. (2017, 2018). A generalized Fokker-Planck equation, allowing for nonlinear regimes, was obtained; its analytical solutions have been validated by results of test particle numerical simulations. Two nonlinear regimes were taken into account: phase bunching (nonlinear scattering) and wave trapping; those regimes cause particles fast transport in phase space in the opposite directions. As a result, the Gaussian-shaped particle distribution function was shown to reach almost isotropic stationary solution. Kubota and Omura (2017) analyzed long time evolution of particle distribution in equatorial pitch angles under the resonant interaction and found echoes of electron depletion by the localized EMIC wave packets with rising frequency. They excluded particles with initial equatorial pitch angles near the loss cone from the consideration to avoid quasi-linear effects.

In this paper, we study the evolution of pitch angle distribution function during several passes of particles through the EMIC wave packet with rising frequency. We take into account particles with low initial equatorial pitch angles (close to the loss cone) and show that such particles play an important and peculiar role in the formation of precipitated flux. We also calculate precipitated fluxes, and compare them with theoretical estimates obtained from quasi-linear equations, and analyze the roles of quasi-linear interaction and several nonlinear regimes in the flux formation.

We show that under sufficiently high but realistic wave amplitude and relatively low refractive index force bunching can be very significant for the particles close to the loss cone. For these particles, force bunching can increase pitch angles and even block the precipitation completely from a noticeable range of low pitch angles. We show that for the most part of the considered parameters the pitch angle distribution in the vicinity of the loss cone is close to isotropic. The precipitating fluxes are formed as a result of several interaction regimes with opposite effects. The simulated fluxes are close to quasi-linear theoretical estimates when these estimates are applicable, and may significantly exceed them in other cases.

Next we describe the simulation model. In section 3.1, we summarize known results about the possible interaction regimes for a single electron pass through the wave packet and apply them to the chosen parameters, and also consider some new aspects of the force bunching. In section 3.2, we discuss the role of various interaction regimes in forming the precipitating flux during multiple passes through the wave packet. In section 4, we discuss the evolution of the pitch-angle distribution, obtain precipitating fluxes and compare the results with theoretical estimates. Section 5 is devoted to discussion and conclusions.

2 Simulation Model

2.1 Theory

For parallel-propagating EMIC waves, the resonant interaction with electrons is possible only at the anomalous cyclotron resonance, and the resonance condition is written as follows:

$$\Delta = \omega - kv_{||} + \Omega_c/\gamma = 0, \tag{1}$$

where ω and k are wave frequency and number, respectively, $v_{||}$ is field-aligned velocity, $\Omega_c = eB_0/mc$, B_0 is geomagnetic field, $e > 0$ is elementary charge, $\gamma = \sqrt{1 + [p/(mc)]^2}$, m and p are the electron rest mass and momentum, respectively.

If the external field inhomogeneity is smooth, the wave magnetic field amplitude, $\mathbf{B}_w$, is small ($B_w \ll B_0$) and wave characteristics vary slowly in time and space on the scales of $2\pi/\Omega_c$ and $2\pi/k$, respectively, the resonant interaction of a test electron with EMIC wave can be described by the following equations:

$$\frac{dW}{dt} = -ev_\perp |E_w| \sin\Psi; \tag{2}$$

$$\frac{dI_\perp}{dt} = -\frac{2e}{mB_0} p_\perp (1 - n_{||}\beta_{||}) |E_w| \sin\Psi; \tag{3}$$

$$\frac{d\Psi}{dt} = -\Delta - \frac{e}{p_\perp}(1 - n_{||}\beta_{||}) |E_w| \cos\Psi; \tag{4}$$

$$\frac{dz}{dt} = \frac{p_{||}}{m\gamma}. \tag{5}$$

Here the subscripts $\perp$ and $||$ denote projections to the transverse and parallel directions with respect to $\mathbf{B}_0$, respectively, E_w is slowly changing wave electric field amplitude, $n_{||} = kc/\omega$, Ψ is the gyrophase defined as the angle between $\mathbf{p}_\perp$ and $-\mathbf{B}_w$, $\beta_{||} = v_{||}/c$, $W = (\gamma - 1)mc^2$ and $I_\perp = p_\perp^2/(mB_0)$ are the electron kinetic energy and the first adiabatic invariant respectively, and z is coordinate along the geomagnetic field with $z = 0$ corresponding to the equator. In the right-hand side of equation (4) the first term represents inertial, or kinematic bunching, while the second one represents the direct influence of Lorentz force on the particle phase (force bunching).

The resonant interaction with EMIC waves, $\omega \ll \Omega_c$, is possible only for $k_{||}v_{||} > 0$ and the change in electron energy W will be insignificant: $\gamma \approx$ const (Bespalov & Trakhtengerts, 1986; Albert & Bortnik, 2009). The interaction result is described by the change in the adiabatic invariant $I_\perp$ or equatorial pitch angle Θ_L, $\mu = \sin^2\Theta_L = (p_\perp^2/p^2)(B_L/B_0)$.

Particle behavior (interaction regime) is determined by the inhomogeneity parameter $\mathcal{R} = \sigma_R R$ (Karpman et al., 1974; Albert, 1993, 2000; Albert & Bortnik, 2009; Kubota & Omura, 2017; Grach & Demekhov, 2018a), where $\sigma_R = \pm 1$ determines the effective inhomogeneity sign, and

$$R = \frac{|d\Delta/dt|}{\Omega_{tr}^2}. \tag{6}$$

Here Ω_{tr}^2 is frequency of electron oscillations in the wave field near the effective potential minimum (Grach & Demekhov, 2018a; Demekhov et al., 2006). Under real conditions, the parameter R changes both in time and in space. These changes are associated both with medium inhomogeneity (including changes in the wave packet frequency and amplitude) and nonlinear changes in the particle parameters during the interaction. However, the main features of the particle motion can be categorized based on the R values calculated at the resonance point in the linear approximation. For $R > 1$, the trajectories of all particles on the phase plane are open (all particles are untrapped), and for $R < 1$ there is a minimum of the wave effective potential, i.e. particle trapping by the

wave field is possible. The phase trajectories of the trapped particles are closed. For resonant interaction of electrons with EMIC wave packet, which is generated near the equator and propagates away from it, the effective inhomogeneity is negative. Hereafter, we assume $\sigma_R = -1$.

The case of $R \gg 1$ corresponds to the quasi-linear regime. In this case the change in particle equatorial pitch angle (and energy) is determined by the resonance phase (Albert, 2000; Albert & Bortnik, 2009; Grach & Demekhov, 2018a):

$$\Delta\mu = K_\mu \sin(\Psi_{\rm res} - \pi/4). \tag{7}$$

Here $\mu = \sin^2\Theta_L$,

$$K_\mu = \frac{2e}{mB_0}|p_\perp(1 - n_{||}\beta_{||})E_{\rm w}|\sqrt{\frac{2\pi}{{\rm d}^2\Psi/{\rm d}t^2}}. \tag{8}$$

All parameters of particles, plasma, and waves in (8) are calculated at the resonance point on the unperturbed trajectory. In the quasi-linear regime, the resonance phase $\Psi_{\rm res}$ linearly depends on the initial phase Ψ_0, so for the particles with initial phases uniformly distributed in $[0, 2\pi]$, $\Psi_{\rm res}$ will also be uniformly distributed in $[0, 2\pi]$. For such ensemble of particles equatorial pitch angle diffusion takes place:

$$\langle\Delta\mu\rangle^{\rm lin} = 0; \tag{9}$$

$$\langle\Delta\mu\rangle^{\rm lin}_{\rm rms} = \sqrt{\langle(\Delta\mu^{\rm lin} - \langle\Delta\mu\rangle^{\rm lin})^2\rangle} = K_\mu/\sqrt{2}. \tag{10}$$

Hereafter, angle brackets denote phase averaging.

For $R \le 1$, the resonant interaction is nonlinear, which leads to drift in pitch angles for both trapped and untrapped particles. The drift direction is determined by the interaction regime and the sign of effective inhomogeneity.

Albert (1993, 2000) have shown analytically that when $R \ll 1$ the resonance phase for untrapped particles can take a limited range of values (for $R \to 0$, $\Psi_{\rm res} \approx \pi$) and the resulting change in particle parameters doesn't depend on the initial phase. For $\sigma_R = -1$, this phase bunching without trapping leads to pitch angle increase (Albert & Bortnik, 2009; Grach & Demekhov, 2018a, 2018b). In some papers (Artemyev et al., 2017, 2018) this regime is called nonlinear scattering. Numerical simulations show (Kubota & Omura, 2017; Grach & Demekhov, 2018a, 2018b) that for not too small $R < 1$ there can exist a small group of untrapped particles whose equatorial pitch angle decreases significantly. This group of particles crosses the separatrix on the phase plane far from the saddle point (near the reflection point), i.e., in the region where the phase is opposite to the phase-bunched particles. The second order resonance condition is approximately fullfilled for these particles (${\rm d}^2\Psi/{\rm d}t^2 \approx 0$), and they spend a long time in the separatrix region, which leads to noticeable pitch angle decrease (detailed analysis of the phase plane can be found in (Grach & Demekhov, 2018a)). We term this regime directed scattering to distinguish it from nonlinear scattering/phase bunching. The third regime is the particle trapping by the wave field. In this case the equatorial pitch angle also significantly decreases.

Nonlinear effects can also take place for $R \ge 1$. For low pitch angles and large K_μ in the case of $K_\mu > \mu$ quasi-linear estimate (7) is inapplicable (or is applicable only for particles with certain initial phases). Force bunching (which is neglected in (7)) also becomes significant for low Θ_L (small μ,i.e., particles near the loss cone). If the wave amplitude is high enough, then the resonance point is shifted during the interaction. It leads to particles with the same initial pitch angle but different initial phases having different resonance points, and, consequently, different values of R and K_μ. If the dependence $K_\mu(\mu)$ is significant, that can cause drift in μ ($\langle\Delta\mu\rangle \ne 0$).

2.2 Wave packet model and plasma parameters

EMIC waves are observed in a wide range of geocentric distances L = 3–10 and longitudes 05–21 MLT (Anderson & Hamilton, 1993; Fraser & Nguyen, 2001; Loto'Aniu et al., 2005; Usanova et al., 2012; Keika et al., 2013). The frequencies of quasi-monochromatic wave packets (pearls or hydromagnetic chorus emissions) are in the range 1–3 Hz. Typical wave amplitudes are about 1–2 nT (Mursula, 2007; Engebretson et al., 2007; Engebretson et al., 2008), but values as large as 11 nT were observed (Engebretson et al., 2015).

In this paper, we consider the wave packets representing hydromagnetic chorus emissions with rising frequency, between the He^+ and proton gyrofrequencies (i.e., in the H^+ band).

The dipole model of geomagnetic field is used with McIlwain parameter $L = 5.69$. Cold plasma density at equator is $N_e = 30$ cm^{-3}, proton density at equator is $N_{H^+} = 0.95N_e$, helium and oxygen densities at equator are $N_{He^+} = N_{O^+} = 0.025N_e = 0.025N_e$.

We consider a single wave packet with initial length along the geomagnetic field line $L_{pt} \approx 4500$ km. The frequency grows linearly from $f_{fe} = 1.025$ Hz ($\approx 0.38f_H$, where f_H is proton gyrofrequency) at the front edge to $f_{te} = 2.3$ Hz ($\approx 0.85f_H$) at the trailing edge $z_{te} \approx -1$ km.

The result of the resonance interaction can significantly depend on the amplitude profile (Tao et al., 2012, 2013; Kubota & Omura, 2017; Grach & Demekhov, 2018a, 2018b). Tao et al. (2012, 2013) discussed the influence of the wave packet fine structure and the role of the subpackets. Here we follow (Grach & Demekhov, 2018a, 2018b), and consider an isolated wave packet with two initial profiles of the magnetic wave amplitude: constant $B_w = B_w^{max} = \text{const}$ (flat packet) and Gaussian-shaped $B_w = B_w^{max}\exp\left(-(z - z_{mp})^2/\sigma_{pt}^2\right)$ (Gaussian packet). Here z_{mp} is the middle point of the packet, maximum initial amplitude is chosen as $B_w^{max} = 3$ nT and $\sigma_{pt} \approx L_{pt}/6$. The Gaussian shape seems more realistic, but we consider both shapes in order to demonstrate the nonlinear effects more clearly and discuss the influence of amplitude profile. The chosen parameters are typical for EMIC events observed by Van Allen Probes in H^+ band (e.g., (Engebretson et al., 2015)) and specifically represent the case observed during a SC event of 14 September 2017, which was discussed by Yahnin et al. (2019).

The packet propagates away from the equator (z is positive and increases). The evolution of the packet (in the cold plasma approximation) is taken into account in the simulation. The simulation time is limited to 6.5 s; at later times the dispersion distortion of the packet due to the presence of He^+ ions becomes significant. This choice of simulation time also allows us to neglect the effect of magnetic drift on the electron distribution function in a given flux tube. Indeed, the typical transverse size of EMIC wave packets known from spaceborne and ground-based measurements is about 2°. For the chosen energy range $W_0 = 1.4$–3.0 MeV, the drift time across the packet will be 17–36 s, which is more than two times longer than simulation time. The energy range is chosen based on R values for Gaussian packet (see below). The initial equatorial pitch angle range is $\Theta_{L0} = 4$–$80°$. From below it is limited by the loss cone (for $L = 5.69$, $\Theta_{Lc} \approx 3.1°$) and from above by the condition of the resonant interaction for particles within the specified energy range. For particles in the considered energy range, the simulation time corresponds to 10–20 bounce periods.

The system (2)–(5) was solved numerically by Bogacky-Shampine variant of the Runge-Kutta method. Calculations were done for 8 values of energy in the specified range (1.4; 1.6; 1.8; 2.0; 2.25; 2.5; 2.75 and 3.0 MeV), 77 values of equatorial pitch angle (step of 1 degree) and 180 values of the initial phase (uniformly in $[0, 2\pi]$). Thus, for every energy, the trajectories of 13860 particles were calculated. At the moment $t = 0$ all particles are placed at the trailing edge of the packet with positive longitudinal velocities. As is shown below, this is insignificant for the results, since the particles are spread over

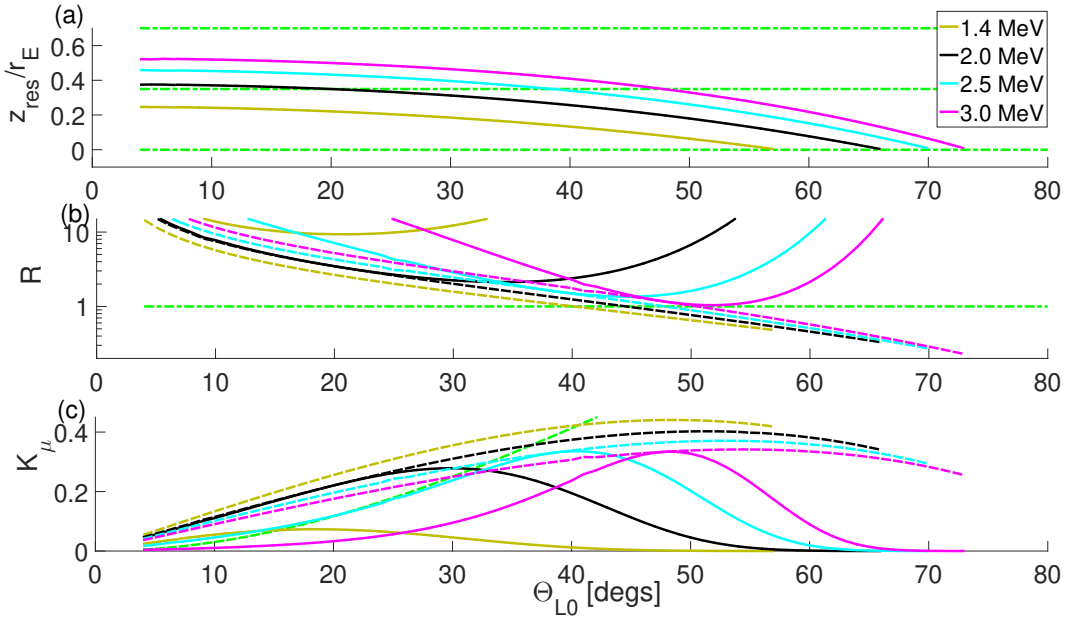

Figure 1. Resonance point location $z_{\rm res}$ normalized to the Earth radii $r_{\rm E}$ (a), unperturbed value of the inhomogeneity parameter R (b), and parameter K_μ (c) for a flat packet (dashed lines) and a Gaussian packet (solid lines). Green dash-dotted lines show the edges and middle of the packet (a), $R = 1$ (b) and the line $K_\mu = \mu$ (c).

the field line in 3–4 bounces. If the particle is in the loss cone after leaving the packet ($\Theta_L < \Theta_{Lc}$), then the simulation for this particle is stopped.

3 Specific features of Interaction Regimes

3.1 Single pass through the wave packet

In this section we will analyze the interaction regimes for a single electron pass through the wave packet. The results of this analysis combined with knowledge of wave packet evolution will allow us to qualitatively understand multi-pass results.

3.1.1 Inhomogeneity parameter

The resonance point locations and the unperturbed values of parameters R and K_μ for various initial equatorial pitch angles and the electron energies are shown in Figure 1 (for the initial packet location, $t = 0$). The values of K_μ are fairly large even for linear conditions ($R > 1$), which results from relatively low plasma density. The latter determines the EMIC wave refractive index entering formula (8).

The resonance point is shifted to the packet trailing edge with increasing Θ_L. For a flat wave packet, the inhomogeneity parameter R decreases with Θ_L and increases with energy W_0, while for a Gaussian wave packet R has a minimum in Θ_L which location depends on particle energy. Parameter K_μ has a maximum in Θ_L, but for a flat packet the K_μ decrease at high Θ_L is insignificant.

Quantitatively, nonlinear regimes $R \leq 1$ for a Gaussian packet can be observed only for highest energies from the considered range and for a narrow pitch angle range near 50°. For a flat packet, $R \leq 1$ regimes can be observed for all energies, but for rel-

atively high pitch angles $\Theta_L > 40°$. At the same time, as the dependence $K_\mu(\Theta_L)$ shows, various nonlinear effects are possible for $R > 1$ at low pitch angles, since the inequality $K_\mu > \mu$ is satisfied in a sufficiently wide pitch angle range (for all energies for a flat packet, for $W_0 < 2.75$ MeV for a Gaussian packet). Also, because wave amplitude is high, the resonant interaction shifts the location of the resonance point: for particles with increasing and decreasing pitch angle the resonance point is shifted to the trailing and front edge of the packet, respectively. Recall that the sign of pitch angle change depends on the initial phase (see Eq.(7)). The value of K_μ in (7) thus will also depend on the initial phase. As can be seen from Figure 1c, for some pitch angles $|\mathrm{d}K_\mu/\mathrm{d}\Theta_{L0}|$ is relatively large, so the effects of the nonlinear shift of the resonance point can be significant.

With packet propagation away from the equator, the resonance points are shifted to higher z, at the same time they become closer to the trailing edge of the packet. The value of R also changes. For a Gaussian packet, propagation away from the equator shifts the location of minimum R to the lower Θ_L and increases its value (for illustration, see (Grach & Demekhov, 2018a)). Consecutively, R decreases for smaller Θ_L and increases for higher Θ_L. For a flat packet, qualitatively the dependence on packet location is the same, but quantitatively it is much weaker.

Due to a fairly high wave amplitude and the packet being relatively short, the region of resonant interaction is determined by the effective packet length. Because of this, resonant interaction with packets with different profiles can yield different results even when resonance points are located in the middle of the packet (where R and K_μ are the same for both packets).

Grach and Demekhov (2018a, 2018b) considered a similar wave packet, but with a higher electron density N_e. This leads to a higher refractive index n which in turn shifts the range of resonant electron energies to lower values and noticeably decreases R. In that case, nonlinear regimes $R \leq 1$ are also possible and effective for a Gaussian wave packet.

3.1.2 Change in pitch angle in different interaction regimes

The possibility and the comparative influence of various interaction regimes can be analyzed based on the phase averaged change of $\mu = \sin^2\Theta_L$. Dependencies $\langle\Delta\mu\rangle(\Theta_L, W_0)$ are shown in Figure 2.

According to Figure 2, various nonlinear regimes ($\langle\Delta\mu\rangle \neq 0$) are possible in a chosen range of parameters. Detailed analysis of particle trajectories shows the following.

For a Gaussian packet, positive $\langle\Delta\mu\rangle$ results from combined effect of force bunching and nonlinear shift of the resonance point under condition $\mathrm{d}K_\mu/\mathrm{d}\Theta_{L0} > 0$. Force bunching dominates for lower pitch angles, when the condition $K_\mu \geq \mu$ is satisfied for $R > 1$, i.e. quasi-linear estimate (7) formally allows pitch angle decrease to the negative values. Under these conditions, force bunching (the second term on the right-hand side of (4), which is enhanced when $p_\perp \to 0$) ensures the physical consistence of the system (2)–(5) solution (the positivity of the first adiabatic invariant) and increases pitch angle during resonant interaction. For initial pitch angles near the loss cone, the influence of force bunching is so strong, that not only the mean value $\langle\Delta\mu\rangle > 0$ but also $\Delta\mu > 0$ for a single particle with an arbitrary initial phase. For this case, the particle trajectories, phase plane and $\Delta\mu(\Psi_\mathrm{res})$ are shown in Figure 3a. Here Ψ_res is the phase at the point of resonance $\Delta = 0$, calculated along the real trajectory. Note that the coefficients of the system (2)–(5) depend on time explicitly, i.e., the system is non-autonomous. Therefore, the trajectories on the phase plane may intersect (different trajectories reach the same point at different times). As one can see, resonance phase can take values from a limited range, and doesn't equal the phase at the point $\mathrm{d}\Psi/\mathrm{d}t = 0$.

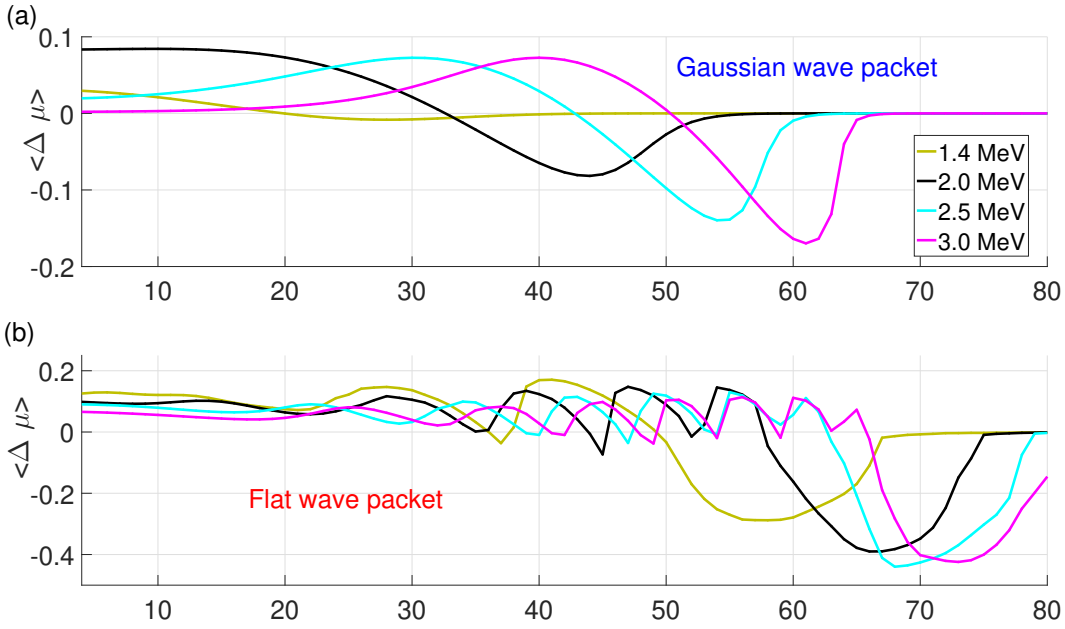

Figure 2. Phase averaged change in μ for Gaussian (a) and flat (b) wave packets.

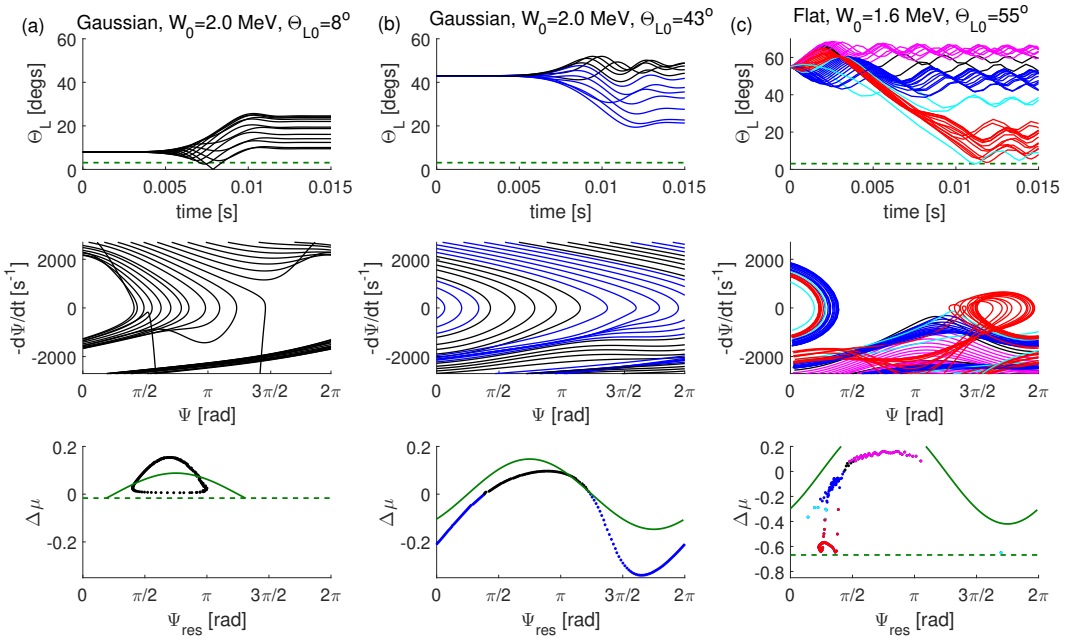

Figure 3. Illustration of the possible interaction regimes. Plots in columns a), b), and c) correspond, respectively, to the force bunching, nonlinear shift of the resonance point, and various regimes at $R < 1$. Top rows show the oscillograms of Θ_L, middle rows show the phase plane, and bottom rows show the $\Delta\mu$ dependence on the resonance phase. Colors denote types of particle trajectories: black and blue correspond to untrapped particles with $\Delta\mu > 0$ and $\Delta\mu < 0$, respectively, magenta to phase-bunched particles, cyan to directed scattering and red to wave trapping. Green dashed lines in the top and bottom rows indicate loss cone, and green solid lines correspond to quasi-linear estimate (7).

In the case when the maximum of $\langle\Delta\mu\rangle(\Theta_{L0})$ is located at the intermediate pitch angles ($W_0 > 2$ MeV), this maximum is caused by the nonlinear shift of the resonance point under condition $\mathrm{d}K_\mu/\mathrm{d}\Theta_{L0} > 0$. The negative values of $\langle\Delta\mu\rangle$ are caused by nonlinear shift of the resonance point under condition $\mathrm{d}K_\mu/\mathrm{d}\Theta_{L0} < 0$, i.e. when change in pitch angle (7) decreases with Θ_{L0}. This case is illustrated by Figure 3b. As one can see, phase portrait of the system is close to the quasi-linear regime, while the dependence $\Delta\mu(\Psi_{\mathrm{res}})$ differs from estimate (7).

Nonlinear regimes corresponding to $R \leq 1$, i.e. phase bunching, directed scattering and particle trapping by the wave field occur for a certain fraction of particles for energies $W_0 \geq 2.5$ MeV in the vicinity of the minimum $\langle\Delta\mu\rangle$ (trapping only takes place for $W_0 = 3.0$ MeV).

For a flat packet, the region of $\Theta_{L0} < 30$–$35°$ corresponds to the combined effect of force bunching and nonlinear shift of the resonance point under condition $\mathrm{d}K_\mu/\mathrm{d}\Theta_{L0} > 0$ (force bunching predominates for lower Θ_{L0}). For the intermediate pitch angles (from 30–50° for $W_0 = 1.4$ MeV to 40–65° for $W_0 = 3.0$ MeV), the main interaction regimes are phase bunching (causes local maxima $\langle\Delta\mu\rangle > 0$) and directed scattering (causes local minima $\langle\Delta\mu\rangle \approx 0$). The smooth global minimum under high Θ_L is caused by the effective wave trapping, though for untrapped particles both phase bunching and directed scattering can take place. This case is shown in Figure 3c. The global minimum of the dependence $\langle\Delta\mu\rangle(\Theta_L)$ for a flat packet corresponds to the unperturbed resonance point located at the trailing edge of the packet. At higher pitch angles, the unperturbed resonance condition is not fulfilled within the packet, but due to nonlinear shift of the resonance point, for some particles the resonance condition can be fullfilled; all such particles are trapped by the wave field. Detailed study of the nonlinear interaction regimes under $R < 1$ can be found in (Grach & Demekhov, 2018a, 2018b).

With increasing electron energy, the local extrema of $\langle\Delta\mu\rangle(\Theta_L)$ are shifted to higher Θ_L, for both packets. Wave packet propagation away from the equator will shift the local extrema of $\langle\Delta\mu\rangle(\Theta_L)$ to the lower Θ_L (same as with $R(\Theta_L), K_\mu(\Theta_L)$).

3.2 Precipitation mechanisms and effects of wave packet propagation

Preliminary analysis of particle trajectories shows that precipitation is possible as a result of either almost quasi-linear interaction, directed scattering or wave trapping. The range of particle pitch angles for which the precipitation in either regime is possible is also influenced by force bunching, nonlinear shift of the resonance point and phase bunching. To study the role of each precipitation mechanism we plot temporal dynamics of 'scattering' equatorial pitch angle $\Theta_{L\mathrm{sc}}$ defined as equatorial pitch angles of precipitating electrons before the last interaction. Similar analysis was made by Kubota and Omura (2017), for different wave packet and plasma parameters, but they did not discuss precipitation for the particles near the loss cone. We also show the distribution of all precipitating particles over $\Theta_{L\mathrm{sc}}$.

3.2.1 Gaussian wave packet

The results for a Gaussian wave packet are shown in Figure 4. For the first 3–4 passes of particles through the wave packet in the resonant direction (which takes about 2 s) the temporal dynamics is influenced by the initial particle distribution in space. Recall that at $t = 0$, the ensemble of the particles is placed at the trailing edge of the wave packet. After that, the particles can be considered uniformly distributed between the mirror points. The initial particle location doesn't influence the distribution of precipitating particles over the scattering pitch angles.

Precipitation is possible only for $\Theta_{L\mathrm{sc}} \leq 28°$. For these values, three regimes are possible: almost quasi-linear regime, force bunching, and nonlinear shift of the resonance

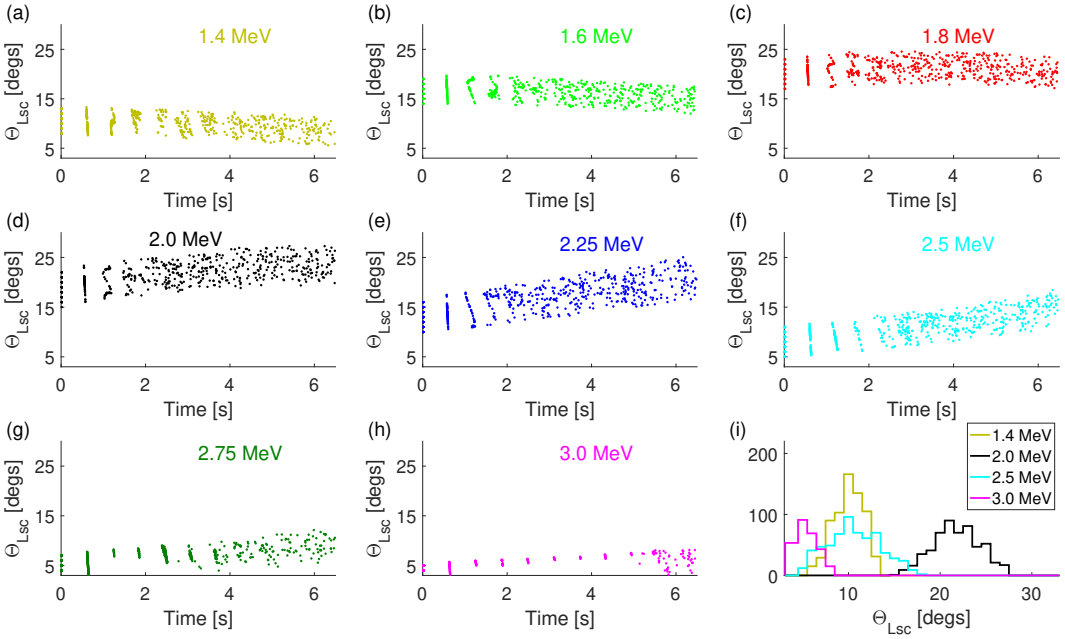

Figure 4. Equatorial pitch angles Θ_{Lsc} of precipitating electrons before the last interaction with the wave packet as a function of time, for a Gaussian wave packet. Time stamps correspond to particle exiting the wave packet, i.e. approximately a one and a quarter of bounce period T_B before precipitating. Panel (i) shows the distribution of precipitating particles over Θ_{Lsc} during the entire simulation interval.

point with $\langle \Delta\mu \rangle > 0$. Nonlinear resonance shift with $\langle \Delta\mu \rangle < 0$ takes place only for $\Theta_L \geq 40°$, which is above Θ_{Lsc} range. That means that precipitation in this regime is not possible, but particles can be effectively moved to the lower pitch angles (see also Figure 3b). As it was mentioned above in Section 3.1.2, the nonlinear regimes under $R \leq 1$ take place only for a small fraction of particles and do not have significant effect.

For particles with energies 1.6–2.25 MeV, the influence of force bunching is strong enough to block precipitation completely for equatorial pitch angles up to $\Theta_L \approx 15°$.

The range of Θ_{Lsc} depends on time for most of the energies. For lower energies, $W_0 = 1.4$–1.6 MeV, resonance points for $\Theta_L < 25°$ at $t = 0$ are located closer to the trailing edge of the packet and for them R increases and K_μ decreases as the packet propagates (at the time $t = 0$, minimum R is located close to the loss cone). Smaller values of K_μ correspond to lower initial pitch angles for which estimate (7) gives decreasing of μ below the loss cone value μ_c (precipitation in quasi-linear regime) or below zero (effective force bunching blocking precipitation). Thus, both maximum and minimum Θ_{Lsc} decrease in this case. For higher energies, $W_0 = 2.0$–3.0 MeV, the situation is the opposite: resonance points for $\Theta_L < 25°$ at $t = 0$ are located closer to the front edge of the packet, thus R decreases (K_μ increases) as wave packet propagates. Thus, both maximum and minimum values of Θ_{Lsc} increase.

Distributions of precipitated particles over Θ_{Lsc} (Figure 4i) have similar profiles for all the energies, i.e., they have a smooth maximum in the middle of the Θ_{Lsc} range.

3.2.2 Flat wave packet

The temporal dynamics of Θ_{Lsc} is shown in Figure 5.

For all energies, there is a small number of particles which are scattered into loss cone having initial pitch angle that differs from Θ_{Lc} by fractions of a degree. The analysis of their trajectories shows that these particles precipitate after non-resonant interaction with the wave packet (due to the large amplitude) to conjugated ionosphere. Their number is small compared to the total number of precipitating particles, and they do not influence any further results.

Force bunching blocks precipitation from low pitch angles for all energies, though its influence (range of 'blocked' pitch angles) decreases with energy and varies with time. Scattering pitch angles $\Theta_{Lsc} < 45$–$50°$ correspond to precipitation after almost quasi-linear interaction or directed scattering. High scattering pitch angles correspond to precipitation directly caused by wave trapping. For the considered parameters of plasma and wave packet, this effect is possible only for energies $W_0 = 1.4$–1.8 MeV; with increasing energy this precipitation starts later in time. It can be explained as follows. For higher energies, the region of effective wave trapping is located at higher Θ_L (see Figure 2b), thus even the same value of $\langle\Delta\mu\rangle$ is not enough for a particle to precipitate. Wave packet propagation shifts the effective wave trapping region to lower pitch angles, which makes precipitation possible.

Distributions of precipitating particles in pitch angles have different profiles for different energies. Apart from the very narrow maximum very close to the loss cone, which corresponds to the particles precipitated after non-resonant interaction, their structure is as follows. For $W_0 = 1.4$–1.8 MeV, the distributions have three local maxima: the first one (near 20°) corresponds to quasi-linear regime, and the second (around 40°) and third (50–70°) ones correspond to directed scattering and wave trapping, respectively. The 'dip' between the second and the third maxima can also be seen on the temporal dynamics panels. It corresponds to the region where phase bunching prevails (recall that phase bunching results in a pitch-angle increase). For energies $W_0 = 2.0$–3.0 MeV, precipitation is mostly caused by quasi-linear regime, though precipitation by directed scattering is also possible for a number of particles.

The smooth variations of scattering pitch angle range (for quasi-linear regime) are connected with fluctuations in $\langle\Delta\mu\rangle(\Theta_L)$; wave packet propagation will shift the local extrema of $\langle\Delta\mu\rangle(\Theta_L)$.

4 Pitch Angle Distribution and Precipitating Fluxes

In the further analysis of the simulation results, the total simulation time 6.5 s is divided into 11 intervals $\{\Delta t_i\} = t_{i+1} - t_i$, $i = 0, 1, ..11$, $t_0 = 0$, where $\Delta t_0 = 0.2$ s and the subsequent intervals $\Delta t_{0<i<11} = 0.6$ s. The latter value corresponds to the bounce period of particles close to the loss cone: $T_{\rm B}(\Theta_L = \Theta_{Lc}) \approx 0.62$–$0.64$ s. Since at the initial time $t = 0$ all electrons are located at the trailing edge of the wave packet, the first time interval $\Delta t_0 = 0.2$ s was chosen sligthly longer than the time $T_{\rm B}(\Theta_L = \Theta_{Lc})/4 \approx 0.15$ s after which a particle near the loss cone reaches the ionosphere. Since $\Delta t_0 < T_{\rm B}(\Theta_L = 80°) \approx 0.33$ s we can say that during Δt_0 all particles passed the wave packet in resonant direction only once. We average the particle distribution function and the precipitating flux over the intervals Δt_i and attribute the obtained result to the time $T_i = (t_{i+1} + t_i)/2$ (the middle of the interval Δt_i).

To analyze the simulation results in terms of particle distribution function and to compare obtained precipitating fluxes with quasi-linear estimates, we have to establish the connection between the distribution function $\Phi_{\Theta_L}(\Theta_L)$ (or $\Phi_\mu(\mu)$) and the distribution of the test particles in the phase space. This procedure is described in detail in the Appendix.

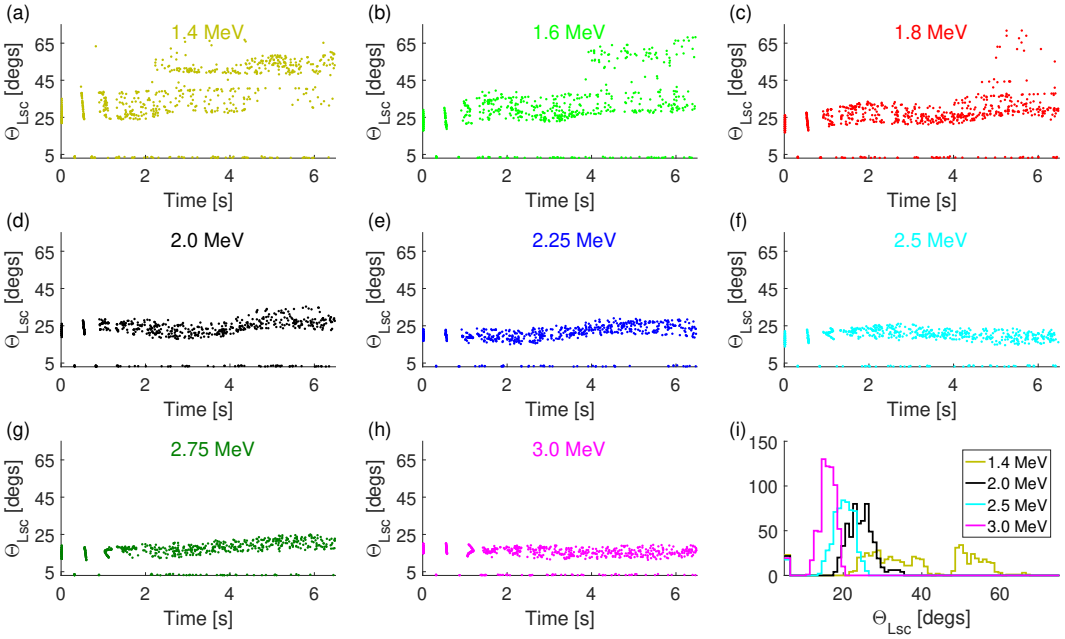

Figure 5. Same as in Figure 4, but for a flat packet.

4.1 Evolution of pitch angle distribution

The particles distribution function $\Phi_{\Theta_L}(\Theta_L)$ for both wave packets for several energy values at several times T_i is shown in Figure 6.

For a flat packet, the distribution function dynamics is qualitatively similar for all the energies considered. For the low equatorial pitch angles near the loss cone, the distribution function is either close to isotropic (with a value slightly lower than the initial value $\Phi^0_{\Theta_L}$; this value decreases slightly with increasing energy), or it has a local maximum in the loss cone. In most cases, the global maximum of the distribution function is located at the pitch angles 60–70° and is equal to the initial value $\Phi_{\Theta_L}(\Theta_L)$ or slightly exceeds it.

For a Gaussian packet, for intermediate energies $W_0 = 1.8$–2.25 MeV and not high pitch angles $\Theta_L \leq 60°$ the distribution function almost coincides with the distribution function for a flat packet. The similar behavior of distribution functions for both packets corresponds to the resonance points for particles with intermediate pitch angles located in the middle of the wave packet. For higher energies 2.75–3.0 MeV, the distribution function increases from small value $\Phi^c_{\Theta_L}$ to the initial value $\Phi^0_{\Theta_L}$ at pitch angles $\Theta_L \approx$ 15–20°. For higher pitch angles, Φ_{Θ_L} fluctuates. For energies 1.4 and 2.5 MeV, at different time moments the distribution function can have a local maximum in the loss cone, be close to isotropic or gradually increase from $\Phi^c_{\Theta_L}$ to the initial value $\Phi^0_{\Theta_L}$.

The main difference between flat and Gaussian wave packets is observed for high pitch angles $\Theta_L > 60°$, because for this range the resonance points are located near the trailing edge of the packet. For a Gaussian packet, due to very small values of wave amplitude at these points there is no resonant interaction for these pitch angles, and the distribution function remains constant. For a flat packet, firstly, small fluctuations of Θ_L are possible even when the exact resonance condition is not fulfilled within the packet, and secondly, due to nonlinear shift of the resonance point, a fraction of particles may be trapped by the wave field, which results in large pitch angle decrease and leads to the appearance of 'dips' in the distribution function in the corresponding region.

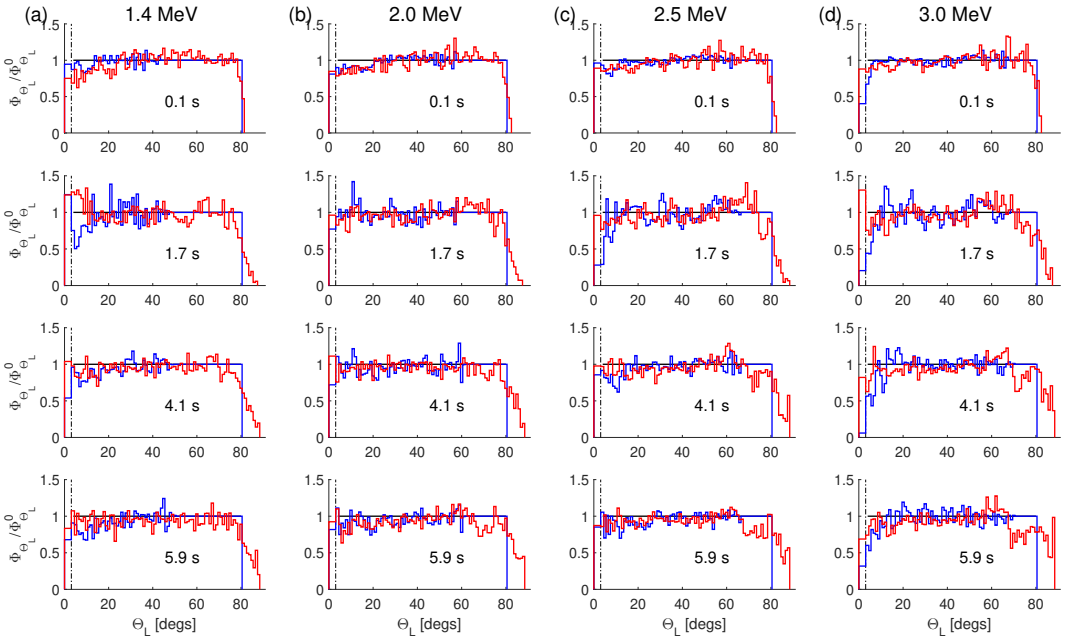

Figure 6. The evolution of pitch angle distribution for a Gaussian packet (blue lines) and a flat packet (red lines). Solid black line shows the initial distribution $\Phi_{\Theta_L}|_{t=0} = \text{const} = \Phi^0_{\Theta_L}$, dash-dotted black line indicates Θ_{Lc}.

4.2 Precipitating fluxes

To analyze the precipitating fluxes $S_{\rm pr}^{\rm num}$, directly corresponding to the numerical simulation results, we normalize them to the flux $S_{\rm pr}^{\rm SD}$ in the limiting case of strong diffusion. In this case the loss cone is filled continuously and distribution function is isotropic; the precipitating flux takes the limiting value equal to the trapped flux (Kennel & Petschek, 1966; Bespalov & Trakhtengerts, 1986; Trakhtengerts & Rycroft, 2008):

$$S_{\rm pr}^{\rm SD} = \frac{N\mu_{\rm c}}{\overline{T}_B}. \tag{11}$$

Here N is the total number of particles in geomagnetic field tube with unit cross section at the ionosphere, $\overline{T}_B = \int T_{\rm B}(\mu){\rm d}\mu$, $\mu_{\rm c}$ corresponds to the loss cone.

In the case when distribution function $\Phi_\mu(\mu)$ is not isotropic and doesn't have maximum in the loss cone (i.e., has a finite positive derivative $\partial\Phi_\mu/\partial\mu$), it is possible to obtain quasi-linear estimates of precipitating fluxes $S_{\rm pr}^{\rm lin}$. For this, we use the smooth approximation $\Phi_\mu^{\rm sm}(\mu)$ of numerically obtained distribution function. The root mean square deviation of μ that determines the diffusion coefficient is calculated using both the analytical estimate (10) and numerical results (A15). Calculation algorithms for both $S_{\rm pr}^{\rm num}$ and $S_{\rm pr}^{\rm lin}$ can be found in the Appendix.

Since for a flat packet the distribution function is either close to isotropic or has a local maximum in the loss cone, quasi-linear estimates of precipitating flux $S_{\rm pr}^{\rm lin}$ were calculated only for a Gaussian packet and only for those times when the derivative of the distribution function in the vicinity of loss cone was not close to zero.

The normalized precipitating fluxes $\widetilde{S}$ are shown in the Figures 7 and 8 for Gaussian and flat packet, respectively. To avoid the influence of the initial spatial bunching of the particles, we exclude the first time interval $\Delta t_0 = 0$–0.2 s and average over several sequent time intervals, when this influence is significant (see Figures 4 and 5).

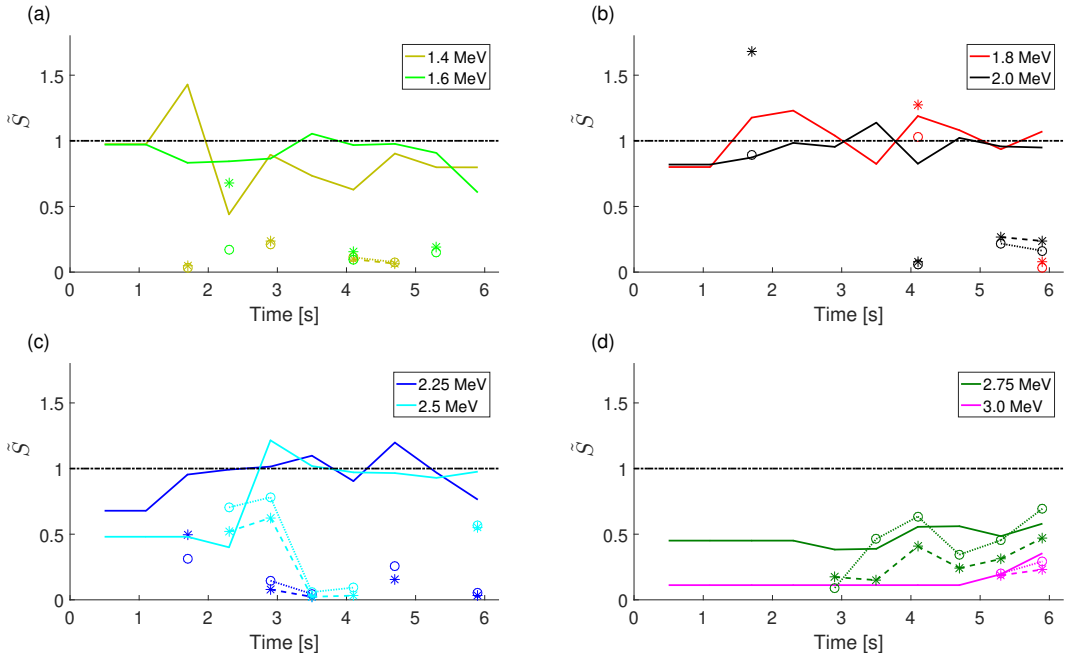

Figure 7. Precipitating fluxes for a Gaussian packet: normalized precipitating flux $S_{\rm pr}^{\rm num}/S_{\rm pr}^{\rm SD}$ (solid lines) and quasi-linear flux $S_{\rm pr}^{\rm lin}/S_{\rm pr}^{\rm SD}$, calculated using diffusion coefficient based on theoretical estimate (10) (dashed lines and star markers) and simulation results (A15) (dotted lines and circle markers).

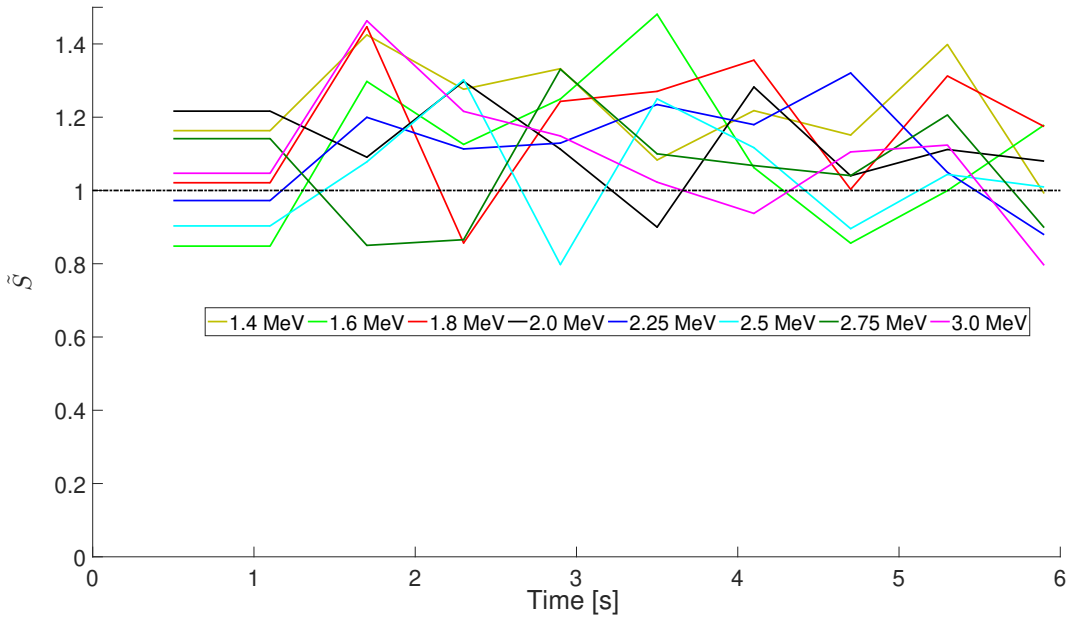

Figure 8. Normalized precipitating fluxes $S_{\rm pr}^{\rm num}/S_{\rm pr}^{\rm SD}$ for a flat packet.

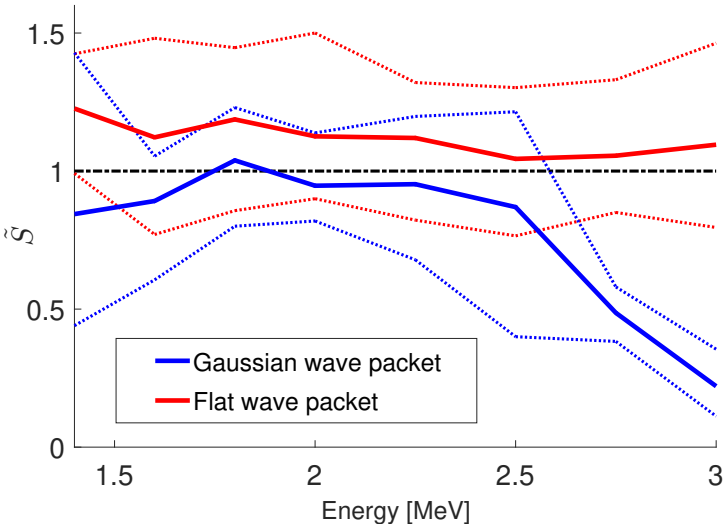

Figure 9. Normalized precipitating fluxes, averaged (solid lines), maximized (dotted lines) and minimized (dotted lines) over the simulation time. Red color corresponds to a flat wave packet, blue color corresponds to a Gaussian wave packet.

The dynamics of precipitating fluxes corresponds to the dynamics of the distribution function. For a flat packet, the flux $S_{\rm pr}^{\rm num}$ fluctuates near the limiting flux $S_{\rm pr}^{\rm SD}$: $S_{\rm pr}^{\rm num} = (0.8\text{–}1.5)S_{\rm pr}^{\rm SD}$. The fluxes exceeding the limiting value correspond to nonmonotonic distribution function having a local maximum in the loss cone.

Precipitating fluxes, averaged over simulation time, as well as maximum and minimum values, are shown in Figure 9. The largest values of $S_{\rm pr}^{\rm num}/S_{\rm pr}^{\rm SD}$ correspond to the energy 1.4 MeV, the smallest ones correspond to 2.5–3.0 MeV. In general, the dependence of maximum/minimum and average fluxes on the energy is weak and nonmonotonic (see Figure 9). Such a dependence clearly indicates the competition between two nonlinear regimes, which have opposite effects on pitch angle dynamics, but the same energy dependence. Recall that force bunching blocks precipitation from low pitch angles, while wave trapping can directly cause precipitation from high pitch angles; the influence of both regimes decreases with increasing energy.

For a Gaussian packet, dependence of normalized flux $S_{\rm pr}^{\rm num}/S_{\rm pr}^{\rm SD}$ on energy and time is much stronger. The maximum values of $S_{\rm pr}^{\rm num}/S_{\rm pr}^{\rm SD}$ correspond to intermediate energies $W_0 = 1.6\text{–}2.0$ MeV. In this case, like in the case of a flat packet, $S_{\rm pr}^{\rm num}$ fluctuates near $S_{\rm pr}^{\rm SD}$, though its maximum values are smaller: $S_{\rm pr}^{\rm num} = (0.8\text{–}1.2)S_{\rm pr}^{\rm SD}$. For lower energy $W_0 = 1.4$ MeV normalized precipitating flux has a maximum over time; for higher energies $W_0 = 2.25\text{–}3.0$ MeV precipitating flux decreases with energy and increases with time (for $W_0 = 2.25\text{–}2.5$ MeV, it quickly increases to $S_{\rm pr}^{\rm num}/S_{\rm pr}^{\rm SD} \approx 1$). This temporal dynamics and dependence on energy follows the dynamics of resonant interaction effectiveness (the value of R) at low ('scattering' range) pitch angles.

In most cases, analytical and numerical values of the root mean square change in μ ((10) and (A15), respectively) are close to each other (see Figure A2). That means that theoretical estimate (10) can be valid even in the case of strong nonlinear effects and $\langle \Delta\mu \rangle \neq 0$. Correspondingly, quasi-linear estimates of the precipitating flux obtained by using either (10) or (A15) give similar results. In contrast to this fact, the fluxes $S_{\rm pr}^{\rm lin}$ are close to the simulated flux $S_{\rm pr}^{\rm num}$ only for energies $W_0 = 2.75\text{–}3.0$ MeV and at some moments for $W_0 = 2.5; 2.0; 1.8$ MeV. Note that the moments with $S_{\rm pr}^{\rm lin} > S_{\rm pr}^{\rm SD}$ (Figure 7b,$W_0 =$ 2.0 and 1.8 MeV) correspond to overestimated analytical diffusion (10) in the case of strong

force bunching (see Figure A2b). In all other cases, $S_{\rm pr}^{\rm lin} \ll S_{\rm pr}^{\rm num}$. The low values of quasi-linear estimates are caused by the following. The smoothed distribution function, which is used for calculating the quasi-linear precipitating flux (see Appendix, Figure A1), in these cases is virtually isotropic, while the original distribution function, obtained in the simulation, has a local maximum in the loss cone, which can't be described by the diffusion equation.

It's interesting to note that for energies $W_0 \leq 2.5$ MeV even in the cases when Φ_μ increases monotonically from the loss cone, quasi-linear estimates can be also much smaller than the fluxes obtained directly from the simulation results. Most likely, it is explained by the following factors. Quasi-linear estimates for the precipitating flux are obtained by the averaging over bounce oscillations; this approach can be used when change in μ during one bounce period (as a result of one resonant interaction) is relatively small. With considered parameters of plasma and wave packets, for energies $W_0 < 2.75$ MeV and low pitch angles (scattering pitch angles range) $\Delta\mu \sim \mu$ and overall number of bounce oscillations is not large. In this case, averaging over bounce oscillations can lead to incorrect results.

5 Discussion and Conclusions

The precipitating fluxes are formed as a result of several interaction regimes with opposite effects. The influence of each regime depends on wave packet characteristics and electron energy.

Under considered parameters of plasma and wave packets, particle trapping by the wave field is not very effective, but the role of nonlinear regimes with inhomogeneity parameter $R \geq 1$ is significant.

The effect of force bunching (the Lorentz force term in Eq. (4) for the particle phase) on the resonant interaction is rarely discussed in analytical studies. Lundin and Shkliar (1977) analyzed motion of resonance electrons with low transverse velocities in the field of a whistler mode parallel propagating wave. They showed that when wave amplitude is high enough, force bunching leads to systematic increase in electron pitch angle. Our simulation shows similar results for electrons interacting with EMIC waves: force bunching leads to pitch angle increase for particles with very low pitch angles near the loss cone. In most part of the considered energy range ($W_0 = 1.6$–2.25 MeV for a Gaussian wave packet and $W_0 < 3$ MeV for the flat wave packet) force bunching blocks the precipitation completely from a noticeable range of equatorial pitch angles (up to 15° and 25° for the Gaussian and flat wave packets, respectively). The significance of the force bunching influence is connected with a relatively low electron plasma density; the latter results in low refractive index, which in turn leads to large change in equatorial pitch angle when $R > 1$ and trapping by the wave field is not possible. Under different plasma conditions, as reported by Kubota and Omura (2017), force bunching can lead to strong equatorial pitch angle decrease for particles released from the wave trapping.

Shift of the resonance point is another nonlinear effect which is important under considered conditions when $R > 1$. For low equatorial pitch angles $\Theta_L \leq 30$–$40°$, nonlinear shift of the resonance point leads to an average increase of the pitch angle. For higher pitch angles, this effect takes place only for a Gaussian wave packet and has the opposite sign, i.e. pitch angle decreases. This decrease does not directly cause precipitation, but particles can be moved to the pitch angles where almost quasi-linear diffusion takes place and precipitation occurs.

Three nonlinear regimes are possible for inhomogeneity parameter $R < 1$: phase bunching (pitch angle increase for a large number of untrapped particles), directed scattering (strong pitch angle decrease for a small number of untrapped particles) and particle trapping by the wave field (also leads to pitch angle decrease in our case). For a Gaus-

sian wave packet and considered parameters, these regimes are possible only for higher energies 2.75–3.0 MeV and in a narrow range of pitch angles, so they do not play a significant role. For a flat wave packet, precipitation as a result of directed scattering and wave trapping is possible for $W_0 = 1.4$–1.8 MeV. For higher energies, directed scattering and wave trapping move particles to the pitch angle range of quasi-linear scattering. Phase bunching blocks precipitation from intermediate equatorial pitch angles and moves particles into the region of effective wave trapping.

It is important to note that, even when the nonlinear precipitation is most effective (flat packet, $W_0 = 1.4$ MeV, see Figure 5), the number of 'nonlinearly' precipitated particles doesn't exceed the number of the particles precipitated in almost quasi-linear regime. The situation will be different for a plasma with higher cold electron density (Kubota & Omura, 2017; Grach & Demekhov, 2018a, 2018b), when the inhomogeneity parameter takes smaller values, and directed scattering and wave trapping are more effective. In that case, nonlinear precipitation will be possible for a Gaussian wave packet (Grach & Demekhov, 2018a, 2018b), and precipitating fluxes will be formed mostly by combined effect of wave trapping and directed scattering (Kubota & Omura, 2017).

To analyze the precipitating fluxes, we have normalized the precipitating fluxes to the flux value in the case of strong diffusion, which corresponds to continuous filling of the loss cone, i.e. isotropic distribution function in the vicinity of the loss cone. Maximum normalized fluxes (in the entire energy range for a flat packet, and $W_0 = 1.8$–2.25 MeV for a Gaussian packet) are close in value and fluctuate near strong diffusion flux. In these cases, distribution function in the vicinity of the loss cone is close to isotropic; there are also moments in which distribution function has a maximum in the loss cone.

For a flat packet, the normalized flux averaged over the simulation time almost doesn't depend on energy. This results from the competition of nonlinear regimes with mutually opposite effects (force bunching and wave trapping) whose strength decreases with energy.

For a Gaussian packet, the time-averaged normalized flux has a maximum over energy. The stronger dependence on particle energy for a Gaussian packet is caused by the different amplitude values at different resonance points. Maximum normalized fluxes are reached for $W_0 = 1.8$–2.25 MeV; in this case, the resonance points for particles with 'scattering' pitch angles are located near the middle of the packet. For lower energies ($W_0 = 1.4$–1.6 MeV) the resonance points for 'scattering' particles are located near the trailing edge of the packet. In this case, the normalized fluxes increase with energy. For higher energies 2.5–3.0 MeV (the resonance points for 'scattering' particles are located near the front edge of the packet) the normalized fluxes increase with time and decrease with energy. The temporal dynamics and energy dependence of the precipitating fluxes and 'scattering' pitch angles range for lower and higher energy follows the dynamics of inhomogeneity parameter R at low ('scattering' range) pitch angles.

The results show that dynamics of nonlinear regimes and their role in the formation of precipitating flux can strongly depend on the amplitude profile of the wave packet. Any difference from the constant amplitude (flat packet) will result in stronger dependence of the precipitating flux on particle energy within the resonant range.

We have compared the precipitating fluxes, obtained in the simulation, with theoretical quasi-linear estimates. For the parameters where quasi-linear equations for the distribution function are applicable, the simulated fluxes are close to theoretical estimates. This is true for higher energies ($W_0 = 2.75$–3.0 MeV) for a Gaussian packet. In other cases, including the ones where precipitating fluxes are formed under $R \geq 1$, i.e., when no trapping is possible, simulated precipitating fluxes exceed theoretical estimates by a factor from 2 to more than 10.

We obtained that pitch angle distribution function is isotropic in the wide range of parameters. This is consistent with observations by low Earth orbit satellites, in which precipitating and trapped fluxes of relativistic electrons are often close or equal to each other (Yahnin et al., 2016, 2017). However, the detailed comparison with the observational data requires a separate study; in particular, the wave packet fine structure has to be taken into account, similar to the approach used by Tao et al. (2012, 2013) for chorus emissions. That study is planned for the future work.

In conclusion, we briefly summarize the main results of this study.

1. The force bunching can completely block the precipitation from low equatorial pitch angles.
2. For the major part of the considered parameter domain, the pitch angle distribution is close to isotropic in the vicinity of the loss cone.
3. The precipitating fluxes are formed as a result of several interaction regimes with opposite effects. For higher energies (2.75–3.0 MeV in the considered case), theoretical quasi-linear estimates are applicable, and the simulated fluxes are close to them. For lower energies, simulated precipitating fluxes exceed theoretical estimates by a factor from 2 to more than 10. This result is important for using quasi-linear diffusion fluxes in numerical modelling of radiation belts.

Appendix A Calculation of the Pitch Angle Distribution Function and Precipitating Fluxes

Most of the expressions below follow Bespalov and Trakhtengerts (1986); Trakhtengerts and Rycroft (2008) and are given here for the reader's benefit.

Let f be the particle distribution function averaged over gyrophases. If the pitch angle and energy change during one bounce oscillation is not very large, then the distribution function F averaged over bounce oscillation period T_B is close to the local distribution function f:

$$F = \frac{1}{T_\mathrm{B}} \int f \mathrm{d}t \approx \frac{1}{T_\mathrm{B}} \int f \frac{\mathrm{d}z}{v_{||}} \approx f. \tag{A1}$$

Total number of particles in a geomagnetic flux tube with unit cross section at the ionosphere can be calculated as

$$N = \int n(z) \frac{B_{0\mathrm{m}}}{B_0(z)} \mathrm{d}z. \tag{A2}$$

Here $n(z) = \int f d^3\mathbf{p} = \int f \sin\Theta \mathrm{d}\Theta\, p^2 \mathrm{d}p\, \mathrm{d}\Psi$ is the local number density, Θ is the local pitch angle, and $B_{0\mathrm{m}}$ is the maximum field for the given geomagnetic field line.

From expressions (A1) and (A2) we can obtain:

$$N = \frac{1}{2\mu_\mathrm{c}} \int 2T_\mathrm{B} F_{\Theta_L}(\Theta_L) \cos\Theta_L \sin\Theta_L \mathrm{d}\Theta_L\, p^2 \mathrm{d}p\, \mathrm{d}\Psi = \frac{1}{2\mu_\mathrm{c}} \int T_\mathrm{B} F_\mu(\mu) \mathrm{d}\mu\, p^2 \mathrm{d}p\, \mathrm{d}\Psi. \tag{A3}$$

Here F_{Θ_L} is the distribution function F written as a function of Θ_L and F_μ is the distribution function F written as a function of μ: $F_{\Theta_L}(\Theta_L) = F_\mu(\mu = \sin^2\Theta_L)$. The value $\mu_\mathrm{c} = \sin^2\Theta_{Lc} = B_{0L}/B_{0\mathrm{m}}$ corresponds to the loss cone.

The particle energy change during the resonant interaction with EMIC waves is insignificant, so we can consider particles with $W_0 = \mathrm{const}$. Then we can use for every energy:

$$F = \frac{\delta(p-p_0)}{p_0^2} \widetilde{F}_{\Theta_L}(\Theta_L, \Psi) = \frac{\delta(p-p_0)}{p_0^2} \widetilde{F}_\mu(\mu, \Psi), \tag{A4}$$

where p_0 is the particle momentum. Integrating (A3) over Ψ and p with account of (A4), we obtain

$$N = \frac{v_0}{2\mu_c}\int \widetilde{\Phi}_{\Theta_L} T_B 2\cos\Theta_L \sin\Theta_L \mathrm{d}\Theta_L = \frac{v_0}{2\mu_c}\int \widetilde{\Phi}_{\mu} T_B \mathrm{d}\mu. \tag{A5}$$

Here $v_0 = p_0/(m\gamma)$,

$$\widetilde{\Phi}_{\Theta_L} = \int \widetilde{F}_{\Theta_L}(\Theta_L, \Psi)\mathrm{d}\Psi; \quad \widetilde{\Phi}_{\mu} = \int \widetilde{F}_{\mu}(\mu, \Psi)\mathrm{d}\Psi. \tag{A6}$$

In order to connect the number N_p of particles in the simulation with N, we use the following normalization:

$$N = \frac{v_0 \overline{T}_B}{2\mu_c}\beta_V N_p, \tag{A7}$$

where $\overline{T}_B = \int T_B(\mu)\mathrm{d}\mu$, β_V is the normalization constant, and N_p is the number of particles in the simulation.

Using (A7), we can write the connection between distribution functions $\widetilde{\Phi}_{\mu}$ and $\widetilde{\Phi}_{\Theta_L}$ and distribution of the test particles in the phase space as follows:

$$\widetilde{\Phi}_{\Theta_L} = \frac{\Delta N_p}{\Delta\Theta_L}\frac{\overline{T}_B}{T_B}\frac{\beta_V}{\sin(2\Theta_L)}; \tag{A8}$$

$$\widetilde{\Phi}_{\mu} = \frac{\Delta N_p}{\Delta\mu}\frac{\overline{T}_B}{T_B}\beta_V. \tag{A9}$$

Here ΔN_p is the number of particles having the pitch angle Θ_L within the range $\Delta\Theta_L$ (in (A8)) and μ in the range of $\Delta\mu$ (in (A9)).

If the initial distribution of test particles in Θ_L is uniform and equal weight is assigned to each particle, then initial distribution function $\widetilde{\Phi}_{\Theta_L}|_{t=0}$ is not constant. At the same time, each particle corresponds to the phase space element $\Delta\Gamma = \sin(2\Theta_L)\Delta\Theta_L\Delta\Psi = \Delta\mu\Delta\Psi$, which does not change during the distribution function evolution. For a more correct analysis of simulation results, instead of the initial function $\widetilde{\Phi}_{\Theta_L}|_{t=0}$ we use the 'weighted' distribution function $\Phi_{\Theta_L}|_{t=0} = \alpha_w(\Theta_{L0})\widetilde{\Phi}_{\Theta_L}|_{t=0} = \mathrm{const}$, where $\alpha_w(\Theta_{L0})$ are the weights assigned to each particle with initial equatorial pitch angle Θ_{L0}. The weights are calculated from the condition that the functions $\Phi_{\Theta_L}|_{t=0}$ and $\widetilde{\Phi}_{\Theta_L}|_{t=0}$ have the same normalization.

To analyze the simulation results we divide the pitch angle values, corresponding to the moments $t_{i+1} < t \le t_i$, $0 \le i \le 11$ into the intervals $\Delta\Theta_{L\,k}$ ($\Delta\Theta_{L\,1} = \Theta_{Lc}, \Delta\Theta_{L\,1,2,\ldots} = 1^\circ$). Every particle is counted with the weight $\alpha_w(\Theta_{L0})$, corresponding to its initial equatorial pitch angle Θ_{L0}. To obtain the value of the distribution function in the loss cone, we count the particles which were scattered in the loss cone during the current time interval Δt_i. The obtained distribution function is attributed to the time $T_i = (t_{i+1} + t_i)/2$.

The effect of quasi-linear pitch angle diffusion on the averaged distribution function is described by the following equation (Bespalov & Trakhtengerts, 1986; Trakhtengerts & Rycroft, 2008):

$$\frac{\partial F_{\mu}}{\partial t} = \frac{1}{T_B}\frac{\partial}{\partial\mu}\left[\mu\overline{D}\frac{\partial F_{\mu}}{\partial\mu}\right]. \tag{A10}$$

Here $\overline{D} = \int D\mathrm{d}t = \int D\mathrm{d}s/v_{||}$, D is the diffusion coefficient, and the integral is taken over the interval of bounce averaging. The diffusion coefficient is calculated as

$$D = \frac{(\langle\Delta\Theta_L\rangle_{\mathrm{rms}})^2}{\Delta t}. \tag{A11}$$

Here $\langle\Delta\Theta_L\rangle_{\mathrm{rms}} = \sqrt{\langle(\Delta\Theta_L - \langle\Delta\Theta_L\rangle)^2\rangle}$ is the root mean square deviation of Θ_L during the time interval Δt. Hence, $\overline{D} = (\langle\Delta\Theta_L\rangle_{\mathrm{rms}})^2$. We consider one wave packet along

the field line, so during a bounce period the particle's pitch angle changes only once, as it passes through the wave packet parallel to the wave.

The simulated precipitating flux is evaluated as:

$$S_{\rm pr}^{\rm num} = \frac{N\delta N_{\rm p}}{\Delta t}. \tag{A12}$$

Here $\delta N_{\rm p} = N_{\rm p\,lost}/N_{\rm p}$ is the relative number of particles, precipitated during time interval Δt.

The particle flux through the loss cone boundary caused by the quasi-linear diffusion can be estimated by integrating (A10) and taking into account the absence of particle sources and sinks at $\mu = 0$ and $\mu = 1$:

$$S_{\rm pr}^{\rm lin} = \frac{v_0}{2}\overline{D}\left.\frac{\partial\Phi}{\partial\mu}\right|_{\mu=\mu_{\rm c}} = \frac{v_0}{2}\frac{(\langle\Delta\mu\rangle_{\rm rms})^2}{4\mu_{\rm c}}\left.\frac{\partial\Phi_\mu}{\partial\mu}\right|_{\mu=\mu_{\rm c}}. \tag{A13}$$

Here $\langle\Delta\mu\rangle_{\rm rms} \approx \sqrt{4\mu(1-\mu)}\langle\Delta\Theta_L\rangle_{\rm rms}$ is root mean square deviation of μ after one resonant interaction in the vicinity of the loss cone $\mu = \mu_{\rm c}$, $\sqrt{1-\mu_{\rm c}} \approx 1$. The derivative $\partial\Phi_\mu/\partial\mu|_{\mu=\mu_{\rm c}}$ can be estimated using distribution function Φ_μ, obtained in the simulation. Analyzing the simulation results, particles with all phase values are summed up, which corresponds to phase averaging.

To obtain distribution function derivative $\partial\Phi_\mu/\partial\mu$, which can be used in (A13), we use a smooth approximation of the numerical distribution function. For a Gaussian wave packet, we choose the following approximation

$$\Phi_\mu^{\rm sm} = \Phi_1 + \Phi_2\tanh[\Phi_3(\mu - \mu^{\rm sm})]. \tag{A14}$$

Coefficients Φ_1, Φ_2, Φ_3 and $\mu^{\rm sm}$ are found by nonlinear least squares method under the conditions $\Phi_2 > 0$ and $\Phi_3 > 0$. To eliminate the influence of the initial spatial distribution of the particles, we average distribution functions Φ_μ over several first time intervals, when such influence is significant (see Figures 4 and 5). Approximation (A14) is shown in Figure A1.

Root mean square deviation $\langle\Delta\mu\rangle_{\rm rms}$ can be calculated in two ways. One approach corresponds to analytical estimate by the stationary phase method $\langle\Delta\mu\rangle_{\rm rms}^{\rm lin}$ (10), and the other approach is based on using the numerical results:

$$\langle\Delta\mu\rangle_{\rm rms}^{\rm num} = \sqrt{\langle(\Delta\mu^{\rm num} - \langle\Delta\mu\rangle^{\rm num})^2\rangle}. \tag{A15}$$

Root mean square deviations, calculated as a function of μ, are shown in Figure A2. For calculating $\langle\Delta\mu\rangle_{\rm rms}^{\rm num}$ (A15), μ is divided in intervals equivalent to step 1° in Θ_L. For every energy W_0 and time moment T_i we find the point μ^*, for which $\langle\Delta\mu\rangle_{\rm rms}(\mu^*) \approx 2(\mu^* - \mu_{\rm c})$ (in Figure A1, these points are shown by vertical lines). To calculate the quasi-linear precipitating flux (A13), we use the diffusion coefficient corresponding to $\langle\Delta\mu\rangle_{\rm rms}(\mu^*)$ and evaluate $\partial\Phi_\mu/\partial\mu$ at μ^* by using (A14).

By analyzing the results for different subsets of particles we found that a numerical uncertainty of our calculations is about 10 %.

Acknowledgments

The study conducted in this paper is theoretical and no data was used. This work was supported by the Russian Science Foundation, grant 15–12–20005.

References

Albert, J. M. (1993). Cyclotron resonance in an inhomogeneous magnetic field. *Physics of Fluids B*, *5*(8), 2744–2750. doi: 10.1063/1.860715

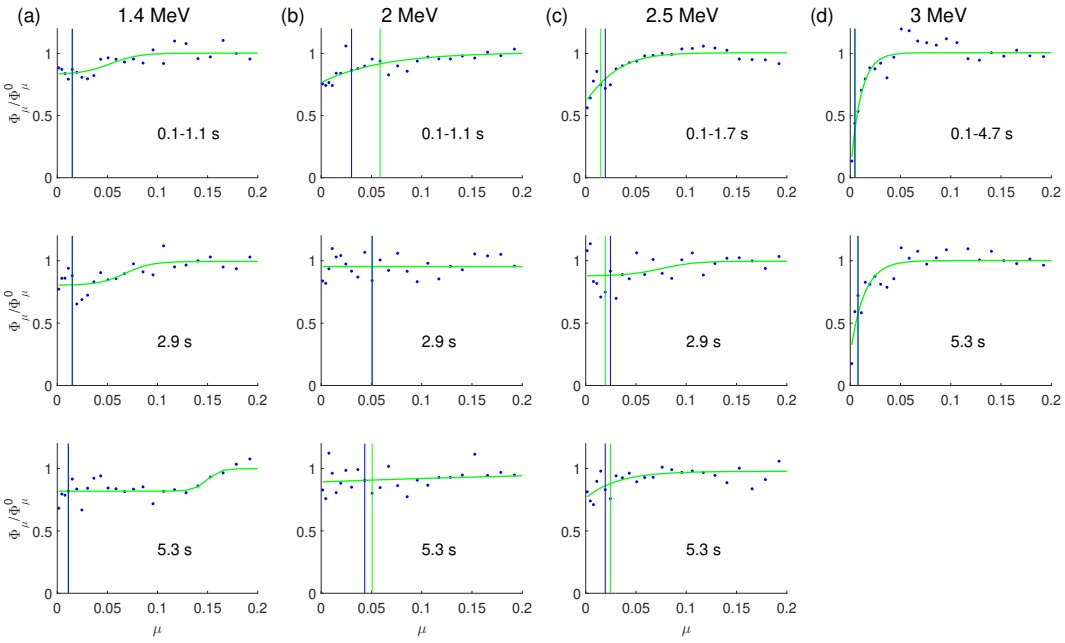

Figure A1. Distribution function, obtained in simulation (blue dots), and approximation (A14) (green lines). Vertical lines correspond to the points μ_*, calculated for $\langle\Delta\mu\rangle^{\rm lin}_{\rm rms}$ (green) and $\langle\Delta\mu\rangle^{\rm num}_{\rm rms}$ (blue). The top panels correspond to distribution function, averaged over several first time intervals.

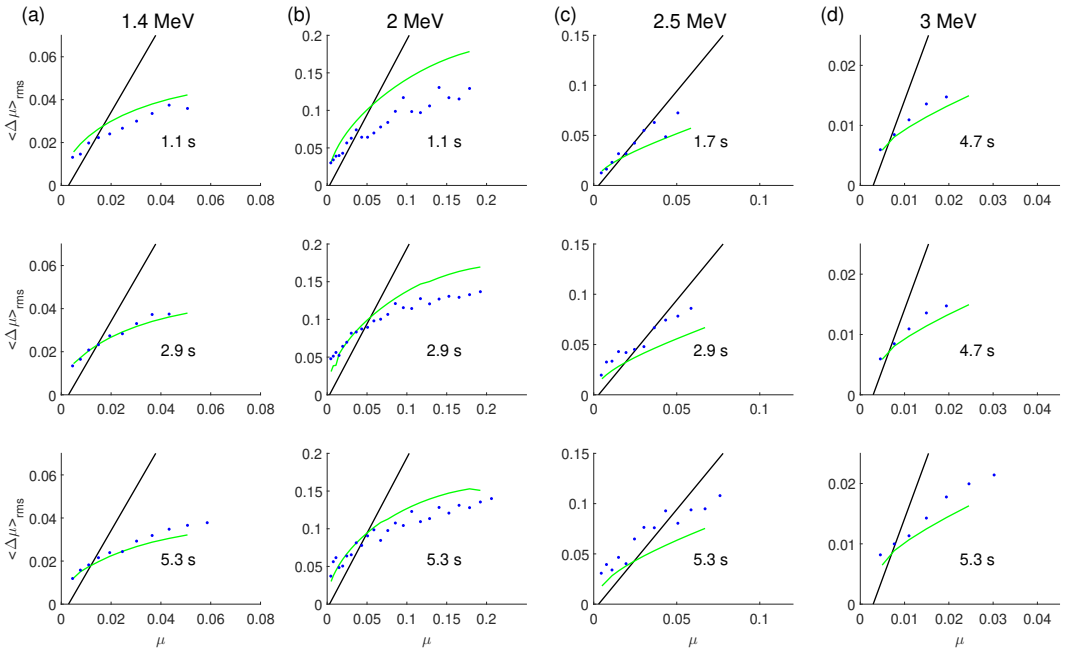

Figure A2. Root mean square deviations $\langle\Delta\mu\rangle^{\rm lin}_{\rm rms}$ (green lines) and $\langle\Delta\mu\rangle^{\rm num}_{\rm rms}$ (blue dots). Black lines correspond to $2(\mu-\mu_{\rm c})$.

Albert, J. M. (2000). Gyroresonant interactions of radiation belt particles with a monochromatic electromagnetic wave. *J. Geophys. Res. Space Physics*, *105*(A9), 21191–21209. doi: 10.1029/2000JA000008

Albert, J. M., & Bortnik, J. (2009). Nonlinear interaction of radiation belt electrons with electromagnetic ion cyclotron waves. *Geophys. Res. Lett.*, *36*(12), L12110. doi: 10.1029/2009GL038904

Anderson, B. J., & Hamilton, D. C. (1993). Electromagnetic ion cyclotron waves stimulated by modest magnetospheric compressions. *J. Geophys. Res. Space Physics*, *98*(A7), 11369–11382. doi: 10.1029/93JA00605

Artemyev, A., Neishtadt, A. I., Vainchtein, D., Vasiliev, A. A., Vasko, I., & Zelenyi, L. (2018). Trapping (capture) into resonance and scattering on resonance: Summary of results for space plasma systems. *Communications in Nonlinear Science and Numerical Simulation*, *65*, 111–160. doi: 10.1016/j.cnsns.2018.05.004

Artemyev, A. V., Mourenas, D., Agapitov, O. V., Vainchtein, D. L., Mozer, F. S., & Krasnoselskikh, V. (2015). Stability of relativistic electron trapping by strong whistler or electromagnetic ion cyclotron waves. *Physics of Plasmas*, *22*(8), 082901. doi: 10.1063/1.4927774

Artemyev, A. V., Neishtadt, A. I., Vasiliev, A. A., & Mourenas, D. (2017). Probabilistic approach to nonlinear wave-particle resonant interaction. *Phys. Rev. E*, *95*(2), 023204. doi: 10.1103/PhysRevE.95.023204

Belyaev, P. P., Kotik, D. S., Mityakov, S. N., Polyakov, S. V., Rapoport, V. O., & Trakhtengerts, V. Y. (1987). Generation of electromagnetic signals at combination frequencies in the ionosphere. *Radiophysics and Quantum Electronics*, *30*(2), 189–206. doi: 10.1007/BF01034491

Belyayev, P. P., Polyakov, S. V., Rapoport, V. O., & Trakhtengerts, V. Y. (1984). Fine structure of Alfven maser radiation. *USSR Report Earth Sciences JPRS UES*, *24*(2), 138.

Bespalov, P. A., & Trakhtengerts, V. Y. (1986). The cyclotron instability in the Earth radiation belts. In M. A. Leontovich (Ed.), *Reviews of plasma physics* (Vol. 10, pp. 155–293). Plenum Publ., N.Y.

Demekhov, A. G. (2007). Recent progress in understanding Pc1 pearl formation. *J. Atmos. Sol. Terr. Phys.*, *69*(14), 1609–1622. doi: 10.1016/j.jastp.2007.01.014

Demekhov, A. G., Trakhtengerts, V. Y., Rycroft, M. J., & Nunn, D. (2006). Electron acceleration in the magnetosphere by whistler-mode waves of varying frequency. *Geomagnetism and Aeronomy*, *46*(6), 711–716. doi: 10.1134/S0016793206060053

Engebretson, M. J., Keiling, A., Fornacon, K.-H., Cattell, C. A., Johnson, J. R., Posch, J. L., ... Rème, H. (2007). Cluster observations of Pc 1 2 waves and associated ion distributions during the October and November 2003 magnetic storms. *Planetary and Space Science*, *55*(6), 829–848. doi: 10.1016/j.pss.2006.03.015

Engebretson, M. J., Posch, J. L., Westerman, A. M., Otto, N. J., Slavin, J. A., Le, G., ... Lessard, M. R. (2008). Temporal and spatial characteristics of pc1 waves observed by st5. *J. Geophys. Res. Space Physics*, *113*(A7), A07206. doi: 10.1029/2008JA013145

Engebretson, M. J., Posch, J. L., Wygant, J. R., Kletzing, C. A., Lessard, M. R., Huang, C.-L., ... Shiokawa, K. (2015). Van Allen probes, NOAA, GOES, and ground observations of an intense EMIC wave event extending over 12 h in magnetic local time. *J. Geophys. Res. Space Physics*, *120*(7), 5465–5488. doi: 10.1002/2015JA021227

Fraser, B. J., & Nguyen, T. S. (2001). Is the plasmapause a preferred source region of electromagnetic ion cyclotron waves in the magnetosphere? *J. Atmos. Sol. Terr. Phys.*, *63*(11), 1225–1247. doi: 10.1016/S1364-6826(00)00225-X

Grach, V. S., & Demekhov, A. G. (2018a). Resonance interaction of relativistic

electrons with ion-cyclotron waves. i. specific features of the nonlinear interaction regimes. *Radiophysics and Quantum Electronics*, *60*(12), 942–959. doi: 10.1007/s11141-018-9860-0

Grach, V. S., & Demekhov, A. G. (2018b). Resonant interaction of relativistic electrons with electromagnetic ion–cyclotron waves. ii. integral parameters of interaction regimes. *Radiophysics and Quantum Electronics*, *61*(6), 389–401. doi: 10.1007/s11141-018-9900-9

Jordanova, V. K., Albert, J., & Miyoshi, Y. (2008). Relativistic electron precipitation by emic waves from self-consistent global simulations. *J. Geophys. Res. Space Physics*, *113*(A3), A00A10. doi: 10.1029/2008JA013239

Kangas, J., Guglielmi, A., & Pokhotelov, O. (1998). Morphology and physics of short-period magnetic pulsations. *Space Science Reviews*, *83*, 435–512.

Karpman, V. I., Istomin, Y. N., & Shklyar, D. R. (1974). Nonlinear theory of a quasimonochromatic whistler mode packet in inhomogeneous plasma. *Plasma Phys.*, *16*(8), 685–703.

Keika, K., Takahashi, K., Ukhorskiy, A. Y., & Miyoshi, Y. (2013). Global characteristics of electromagnetic ion cyclotron waves: Occurrence rate and its storm dependence. *J. Geophys. Res. Space Physics*, *118*(7), 4135–4150. doi: 10.1002/jgra.50385

Kennel, C. F., & Petschek, H. E. (1966). Limit on Stably Trapped Particle Fluxes. *J. Geophys. Res.*, *71*(1), 1–28. doi: 10.1029/JZ071i001p00001

Kubota, Y., & Omura, Y. (2017). Rapid precipitation of radiation belt electrons induced by emic rising tone emissions localized in longitude inside and outside the plasmapause. *J. Geophys. Res. Space Physics*, *122*(1), 293–309. doi: 10.1002/2016JA023267

Loto'Aniu, T. M., Fraser, B. J., & Waters, C. L. (2005). Propagation of electromagnetic ion cyclotron wave energy in the magnetosphere. *J. Geophys. Res. Space Physics*, *110*(A7), A07214. doi: 10.1029/2004JA010816

Lundin, B. V., & Shkliar, D. R. (1977). Interaction of electrons with low transverse velocities with VLF waves in an inhomogeneous plasma. *Geomagnetism and Aeronomy*, *17*(2), 246–251.

Millan, R. M., & Thorne, R. (2007). Review of radiation belt relativistic electron losses. *J. Atmos. Sol. Terr. Phys.*, *69*(3), 362–377. doi: 10.1016/j.jastp.2006.06.019

Morley, S. K., Friedel, R. H. W., Cayton, T. E., & Noveroske, E. (2010). A rapid, global and prolonged electron radiation belt dropout observed with the global positioning system constellation. *Geophys. Res. Lett.*, *37*(6), L06102. doi: 10.1029/2010GL042772

Mursula, K. (2007). Satellite observations of Pc 1 pearl waves: The changing paradigm. *J. Atmos. Sol. Terr. Phys.*, *69*(14), 1623–1634. doi: 10.1016/j.jastp.2007.02.013

Omura, Y., Pickett, J., Grison, B., Santolik, O., Dandouras, I., Engebretson, M., ... Masson, A. (2010). Theory and observation of electromagnetic ion cyclotron triggered emissions in the magnetosphere. *J. Geophys. Res. Space Physics*, *115*(A7), A07234. doi: 10.1029/2010JA015300

Omura, Y., & Zhao, Q. (2012). Nonlinear pitch angle scattering of relativistic electrons by emic waves in the inner magnetosphere. *J. Geophys. Res. Space Physics*, *117*(A8), A08227. doi: 10.1029/2012JA017943

Omura, Y., & Zhao, Q. (2013). Relativistic electron microbursts due to nonlinear pitch angle scattering by emic triggered emissions. *J. Geophys. Res. Space Physics*, *118*(8), 5008–5020. doi: 10.1002/jgra.50477

Pickett, J. S., Grison, B., Omura, Y., Engebretson, M. J., Dandouras, I., Masson, A., ... Constantinescu, D. (2010). Cluster observations of EMIC triggered emissions in association with Pc1 waves near Earth's plasmapause. *Geophys. Res. Lett.*, *37*(9), L09104. doi: 10.1029/2010GL042648

Santolik, O., Gurnett, D., Pickett, J., Parrot, M., & Cornilleau-Wehrlin, N. (2003). Spatio-temporal structure of storm-time chorus. *J. Geophys. Res. Space Physics*, *108*(A7), 1278. doi: 10.1029/2002JA009791

Shoji, M., Omura, Y., Grison, B., Pickett, J., Dandouras, I., & Engebretson, M. (2011). Electromagnetic ion cyclotron waves in the helium branch induced by multiple electromagnetic ion cyclotron triggered emissions. *Geophys. Res. Lett.*, *38*(17), L17102. doi: 10.1029/2011GL048427

Shprits, Y. Y., Chen, L., & Thorne, R. M. (2009). Simulations of pitch angle scattering of relativistic electrons with mlt-dependent diffusion coefficients. *J. Geophys. Res. Space Physics*, *114*(A3), A03219. doi: 10.1029/2008JA013695

Summers, D., & Thorne, R. M. (2003). Relativistic electron pitch-angle scattering by electromagnetic ion cyclotron waves during geomagnetic storms. *J. Geophys. Res. Space Physics*, *108*(A4), 1143. doi: 10.1029/2002JA009489

Tao, X., Bortnik, J., Albert, J. M., Thorne, R. M., & Li, W. (2013). The importance of amplitude modulation in nonlinear interactions between electrons and large amplitude whistler waves. *J. Atmos. Sol. Terr. Phys.*, *99*, 67–72. (Dynamics of the Complex Geospace System) doi: 10.1016/j.jastp.2012.05.012

Tao, X., Bortnik, J., Thorne, R. M., Albert, J. M., & Li, W. (2012). Effects of amplitude modulation on nonlinear interactions between electrons and chorus waves. *Geophys. Res. Lett.*, *39*(6), L06102. doi: 10.1029/2012GL051202

Thorne, R. M., & Kennel, C. F. (1971). Relativistic electron precipitation during magnetic storm main phase. *J. Geophys. Res.*, *76*(19), 4446–4453. doi: 10.1029/JA076i019p04446

Trakhtengerts, V., & Demekhov, A. (2007). Generation of Pc 1 pulsations in the regime of backward wave oscillator. *J. Atmos. Sol. Terr. Phys.*, *69*(14), 1651–1656. doi: 10.1016/j.jastp.2007.02.009

Trakhtengerts, V. Y. (1995). Magnetosphere cyclotron maser: Backward wave oscillator generation regime. *J. Geophys. Res.*, *100*(A9), 17205–17210. doi: 10.1029/95JA00843

Trakhtengerts, V. Y., & Rycroft, M. J. (2008). *Whistler and Alfvén mode cyclotron masers in space*. New York: Cambridge University Press.

Usanova, M. E., Mann, I. R., Bortnik, J., Shao, L., & Angelopoulos, V. (2012). Themis observations of electromagnetic ion cyclotron wave occurrence: Dependence on ae, symh, and solar wind dynamic pressure. *J. Geophys. Res. Space Physics*, *117*(A10), A10218. doi: 10.1029/2012JA018049

Yahnin, A. G., Titova, E. E., Demekhov, A. G., Yahnina, T. A., Popova, T. A., Lyubchich, A. A., ... Raita, T. (2019). Simultaneous observations of elf/vlf and emic waves and energetic particle precipitation during multiple magnetospheric compressions. *Geomagnetism and Aeronomy*, *59*(6), 668–680.

Yahnin, A. G., Yahnina, T. A., Raita, T., & Manninen, J. (2017). Ground pulsation magnetometer observations conjugated with relativistic electron precipitation. *J. Geophys. Res. Space Physics*, *122*(9), 9169-9182. doi: 10.1002/2017JA024249

Yahnin, A. G., Yahnina, T. A., Semenova, N. V., Gvozdevsky, B. B., & Pashin, A. B. (2016). Relativistic electron precipitation as seen by noaa poes. *J. Geophys. Res. Space Physics*, *121*(9), 8286–8299. doi: 10.1002/2016JA022765